Electronic Supplementary Material (ESI) for Physical Chemistry Chemical Physics.

Supporting Information

Two-dimensional MXene/BN van der Waals Heterostructure as Anode Materials for Lithium-Ion Batteries

Kun Yuan [†] *Pengju Hao* [†] *Yang Zhou* [*, †] *Xianchao Hu* [‡] *Jianbo Zhang* [†] *Shengwen Zhong* [*, †]

([†] Faculty of Materials Metallurgy and Chemistry, Jiangxi University of Science and Technology, Ganzhou 341000, PR China

[‡] Research Center of Analysis and Measurement, Zhejiang University of Technology, Hangzhou 310032, PR China)

***E-mail:** yangzhou1998@126.com

1. EXPERIMENTAL SECTION

1.1 Preparation of the delaminated $Ti_3C_2T_x$ Mxene

The commercial Ti_3AlC_2 powder was purchased from 11 Technology Co., Ltd (Jilin, China). The layered Ti_3AlC_2 was chemically etched to remove the Al layer by wet etching as follows: 1 g of LiF was introduced into a Teflon beaker containing 20 mL of 9 M HCl solution under magnetic stirring for 30min. Subsequently, 1 g of Ti_3AlC_2 powder was slowly added into the above Teflon beaker to avoid overheating. Afterward, the etching reaction was conducted at 35 °C under magnetic stirring for 36 h. Next, the resultant product was harvested by centrifugation and washed with deionized water several times until the pH reached at ~6. Finally, 100 mL of deionized water was added to the precipitate and ultrasonicated for 1 h to peel off the multilayer $Ti_3C_2T_x$ into the single layers. The solution was then centrifuged at 3500 rpm for 1 h to separate the monolayer flakes from the multilayer $Ti_3C_2T_x$ and the unreacted MAX. The exfoliated $Ti_3C_2T_x$ used in this study was present in the supernatant after centrifugation. Therefore, the MXene sample used in this experiment can be obtained by putting the supernatant obtained in the above experiment into a beaker and drying it in a freeze dryer for 56 h.

1.2 Preparation of BN nanosheets (BNNSs)

During the experiment, 1g of BN powder was mixed and stirred with 25 ml of H_2SO_4 (95~98%, w/w), then 0.5g of $KMnO_4$ was added slowly to the above solution, and the reaction vessel was placed in an ice bath with continuous stirring. After 12 h, 10 ml of H_2O_2 (30%, w/w) was added dropwise to the mixed solution. Subsequently, the resulting solution was centrifuged at 3000 rpm for 10 min to remove larger reactants, and the supernatant was washed with deionized water and filtered until the pH of the filtrate was 7. Finally, the obtained precipitate was placed in a vacuum drying oven at 40° C for 24 h to obtain the desired boron nitride nanosheets.

1.3 Synthesis of q-$Ti_3C_2T_x$/BNNSs heterojunctions

The delaminated $Ti_3C_2T_x$, boron nitride nanosheets and the mixture with a mass ratio of 9:1 above was respectively placed in a vacuum ball milling tank and ball milling at 500 rpm for 12 hours. After the grinding, it was calcined at 300°C for 3 h at a heating rate of 2 °C/min in an inert atmosphere. The as-prepared product was designated as q-$Ti_3C_2T_x$/BNNSs, respectively. For comparison, the delaminated and multilayer $Ti_3C_2T_x$ was also prepared in the same procedure as above, which was denoted as delta-$Ti_3C_2T_x$ and multi-$Ti_3C_2T_x$.

1.4 Electrochemical measurements

As for the lithium-ion battery tests, all of the CR2032-type coin cells were assembled in an Ar-filled glove box. The working electrode was prepared by mixing the MXene-based samples, acetylene black, and polyvinylidene fluoride (PVDF) in N-methyl-2-pyrrolidinone (NMP) with a weight ratio of 6:2:2. Using a copper foil with a diameter of 14 mm and a thickness of about 8 microns as the current collector, the coated pole piece was placed in an oven at 120°C for 20 min and then rolled under a pressure of 5-10 MPa. Lithium foil was used as counter electrode, Celgard polypropylene as separators and 1 M $LiPF_6$ in ethylene carbonate (EC) and dimethyl carbonate (DMC) a volumetric ratio of 1:1 as the electrolyte. All electrochemical performance tests were conducted under 25 ℃. Cyclic voltammetry experiments were performed by LAND CT2001A battery testing system at a scan rate of 0.1 mV s^{-1}

between 0.05 and 3 V. In addition, CV tests at different scan rates of 0.1~3mV s^{-1} were also performed at a voltage of 0.05~3V to verify the capacitance behavior in the q-$Ti_3C_2T_x$/BNNSs electrode materials. Electrochemical impedance spectroscopy (EIS) measurements were performed using an AC amplitude of 10 mV and a frequency range of 200 kHz to 0.01 Hz.

1.5 Characterization

The morphology and structural information were conducted by SEM (SU-8020, Hitachi) and TEM (JEOL JEM-2100F). The XRD patterns were collected on a Bruker D8 diffractometer (Cu Kα radiation, $\lambda = 1.5406$ Å). The element surface analysis was carried out by XPS (Axis Ultra DLD, Kratos Analytical) with Al Kα radiation. The specific surface area of the sample was determined by N_2 absorption at 77 K with a BeiShiDe 3H-2000PM1 instrument. The Raman spectra were collected on a Raman spectrometer (Labram-010) using 532 nm laser.

2. COMPUTATIONAL METHODS

All calculations were performed with the commercial VASP software, which was based on density functional theory. The Perdew-Burke-Ernzerh (PBE) function with generalized gradient approximation (GGA) was used to describe the interaction between nuclei and electrons. An energy cutoff of 500 eV was used for the plane-wave expansion of the electronic wave function. The valence electronic states of $3s^23p^63d^34s^1$ for Ti, $2s^22p^2$ for C, $2s^22p^4$ for O, $2s^22p^1$ for B, $2s^22p^3$ for N and $1s^22s^1$ for Li were taken into account. The force and energy convergence parameters were set at 0.02 eV/Å and 10^{-5} eV, respectively. Considering that we dealt with weakly interacting systems, the van der Waals (vdw) interactions were taken into account using the semiempirical DFT-D2 approach.

The optimized in-plane lattice constants were 2.51 and 2.98 Å for BN and $Ti_3C_2O_2$ monolayers, respectively, which were consistent with the previous studies. Given that the lattice mismatch between BN and $Ti_3C_2O_2$ was rather small (<5%), the heterostructures composed of 6 × 6 supercell of BN and 5 × 5 supercell of $Ti_3C_2O_2$ were established (see Figure S1). The difference between $Ti_3C_2O_2$ and BN was that $Ti_3C_2O_2$ showed metallic properties with some bands across the Fermi level, whereas BN was an insulator with a large bandgap of 5.9 eV. Moreover, the integration between $Ti_3C_2O_2$ and BN could significantly improve the conductivity of BN, which was desirable for high-rate charging/discharging.

The adsorption energy calculation formula was shown as follows:

$$E_{ads} = E_{all} - E_{surface} - E_{adsorbate}$$

where E_{all}, $E_{surface}$, and $E_{adsorbate}$ represented the total energies of the Li-adsorbed $Ti_3C_2O_2$/BN heterostructure, the pristine heterostructure and the isolated Li atom, respectively. When the adsorption energy was negative, it indicated that the adsorption process was exothermic and the heterostructure of adsorbed Li was energetically stable.

To orientate the minimum energy path and transition states, the climbing image nudged elastic band (CINEB) path was first constructed by linear interpolation of the atomic coordinates and then relaxed until the forces on all atoms were < 0.02 eV/Å. For the large supercell adopted in NEB calculations, only the Γ point was adopted for k-point sampling to reduce the computational cost. The zero-point-energy (ZPE) corrections were applied to all reported energies.

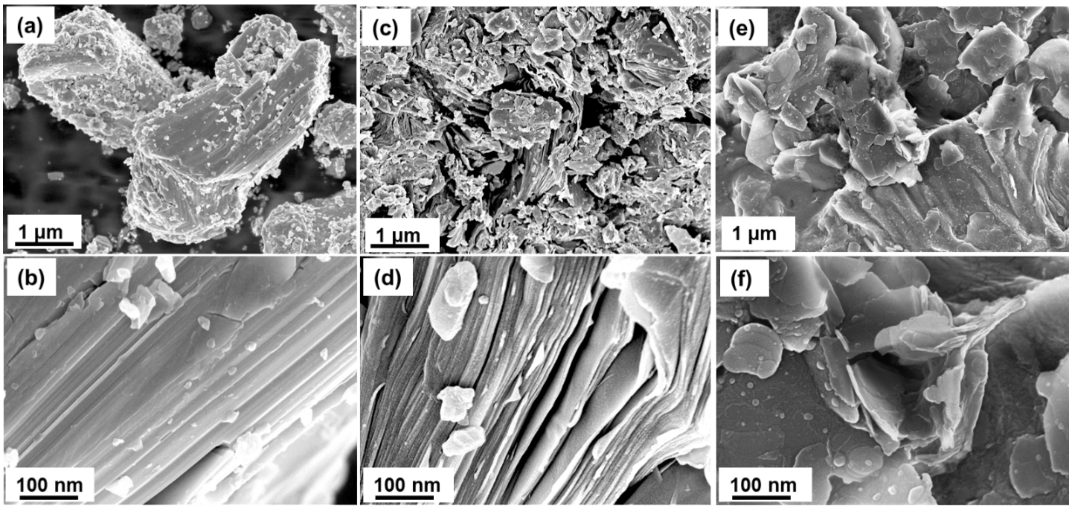

Figure S1. SEM images of (a-b) Ti_3AlC_2, (c-d) $Ti_3C_2T_x$ and e-f) BNNSs

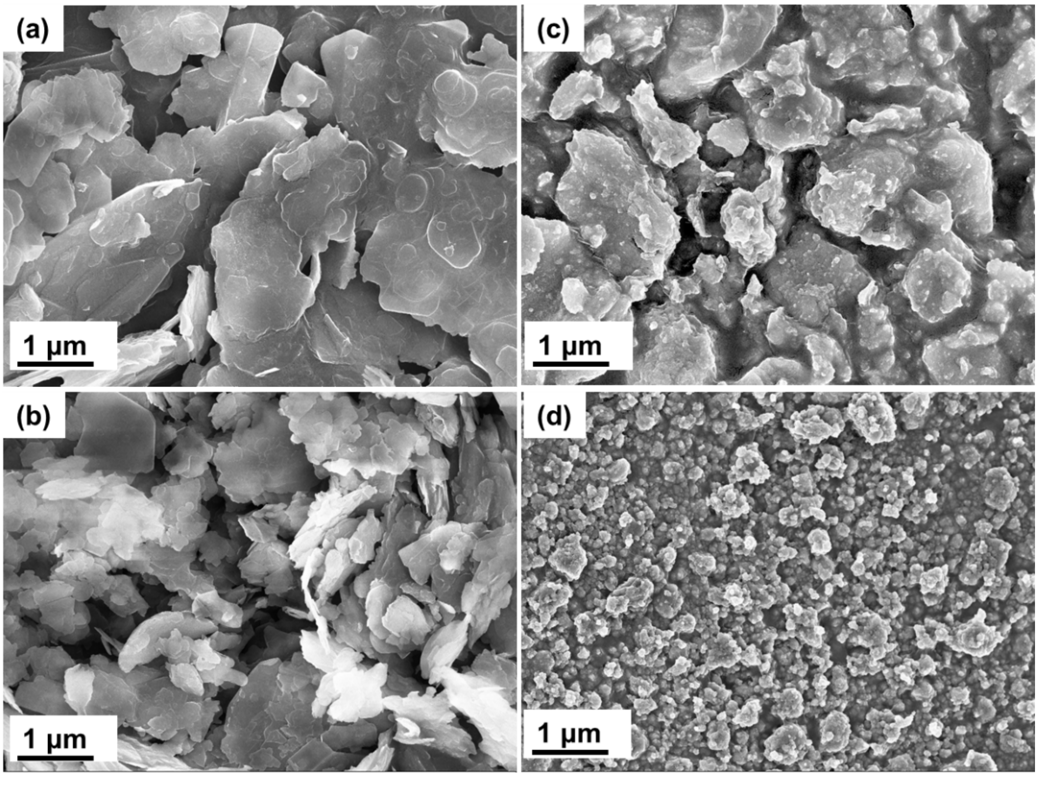

Figure S2. SEM images of (a) BNNSs before ball-milling, (b) BNNSs after ball-milling, (c) $Ti_3C_2T_x$ before ball-milling, (d) $Ti_3C_2T_x$ after ball-milling.

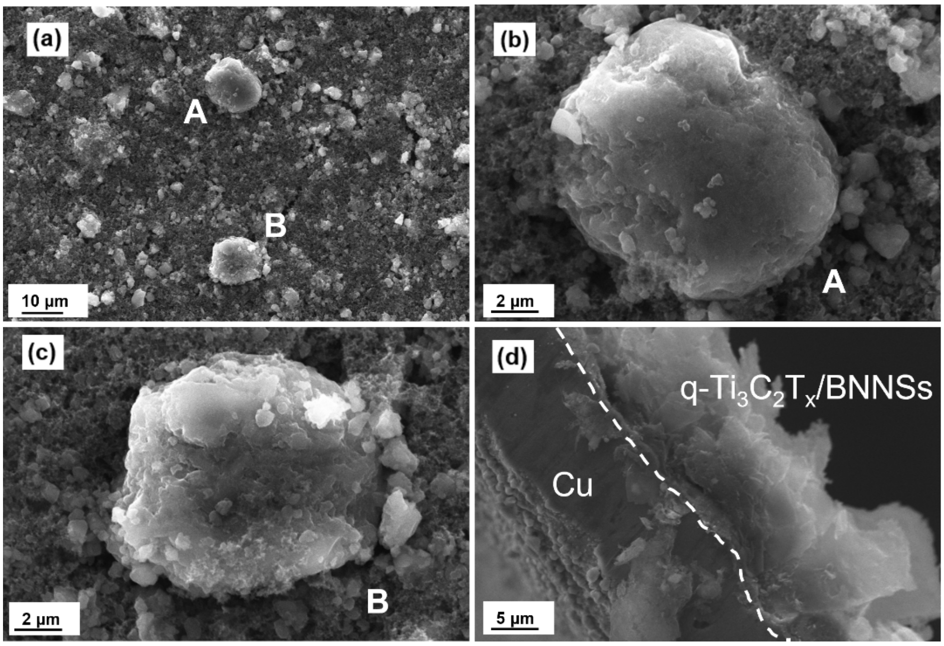

Figure S3. SEM images of q-$Ti_3C_2T_x$/BNNSs in the composite anode.

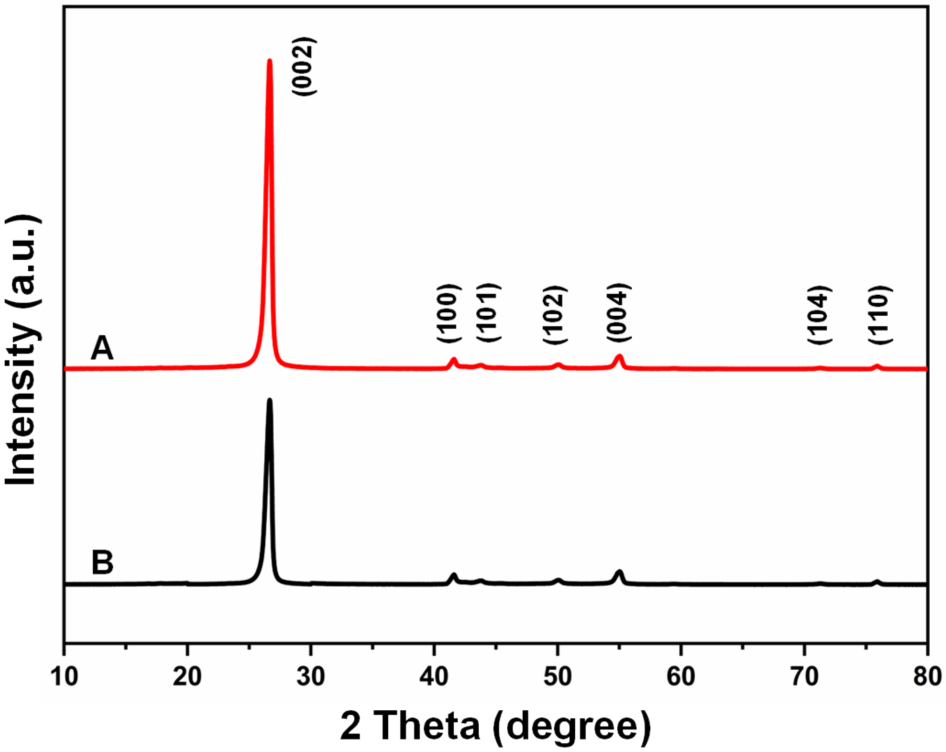

Figure S4. X-ray diffraction pattern of BNNSs (A) and BN powder (B).

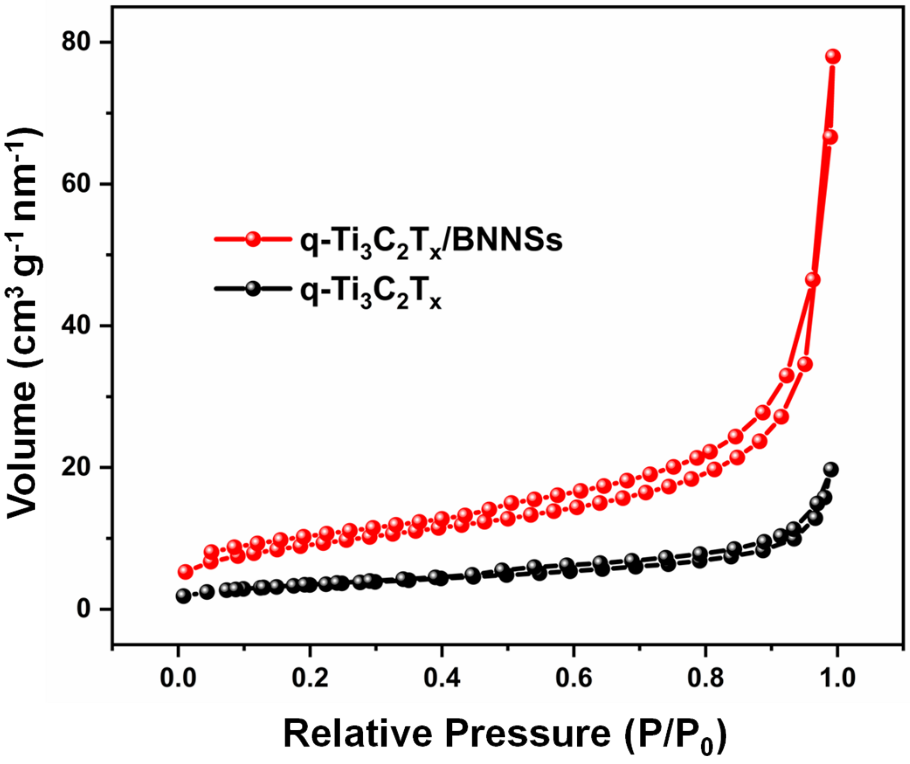

Figure S5. N_2 adsorption/desorption isotherms of q-$Ti_3C_2T_x$/BNNSs and q-$Ti_3C_2T_x$.

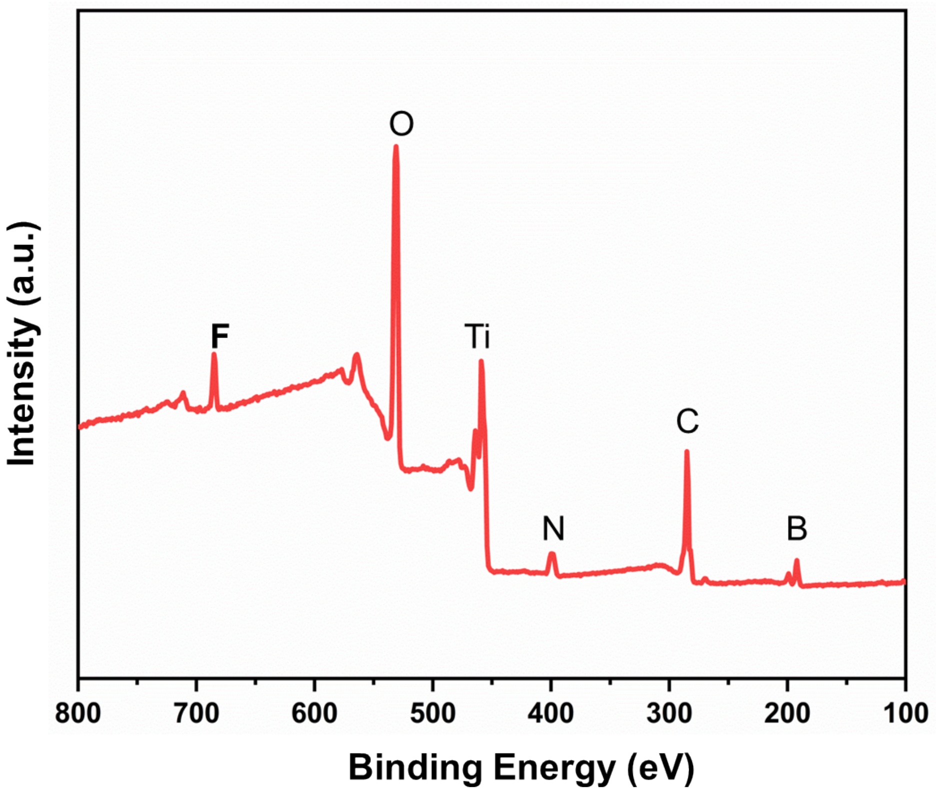

Figure S6. XPS full spectrum of q-$Ti_3C_2T_x$/BNNSs

Table S1. EIS fitting data of the q-$Ti_3C_2T_x$/BNNSs, delta-$Ti_3C_2T_x$, multi-$Ti_3C_2T_x$.

Sample	**Rs**	**CPE**		**Rct**	**Zw**		
	(ohm)	CPE-T	CPE-P	(ohm)	W-R	W-T	W-P
q-$Ti_3C_2T_x$/BNNSs	6.651	0.0001196	0.72579	30.07	15439	76.9	0.8450
delta-$Ti_3C_2T_x$	4.405	2.4932E-5	0.56904	48.13	80.36	2.46	0.3214
multi- $Ti_3C_2T_x$	11.64	0.2974E-5	0.73934	100.6	1633	67.3	0.5028

Table S2. Summary of electrochemical performance of different Ti-based MXene lithium-ion batteries

Material samples	**MXene role**	**Performance**	**Ref.**
q-BNNSs/ $Ti_3C_2T_x$	**Active materials**	**521.6 mAh g^{-1} at 0.1 A g^{-1}** **251.3 mA h g^{-1} at 2.5 A g^{-1}**	**This paper**
$Ti_3C_2T_x$ MXene films	Active materials	115 mAh g^{-1} at 0.5 A g^{-1}	[1]
Ti_3C_2/CNF	Active materials	320 mAh g^{-1} at 1 C	[2]
TiO_2@$Ti_3C_2T_x$	Active materials	124 mAh g^{-1} at 0.05 A g^{-1}	[3]
$Mo_2TiC_2T_x$	Active materials	265 mAh g^{-1} at 0.1 C	[4]
Ti_3CN MXene	Active materials	174 mAh g^{-1}at 0.5 A g-1	[5]
Ti_3C_2-rGO	Active materials	335.5 mAh g^{-1}at 0.05 A g^{-1}	[6]
DES-Ti_3C_2	Active materials	211 mAh g^{-1} at 0.5 A g^{-1}	[7]
Ti_3C_2/TiO_2/rGO	Active materials	176 mA h g-1 at 1 A g^{-1}	[8]
$Ti_3C_2T_x$	Active materials	5.9 mAh cm^{-1} at C/3	[9]
MXene-H_2	Active materials	127 mAh cm^{-1} at 1C	[10]
BPQDs/Ti_3C_2	Active materials	167 mAh g-1 at 2 A g^{-1}	[11]
$MoSe_2$/MXene@C	Active materials	355 mA h g^{-1} at 0.2 A g^{-1}	[12]

SnO_2-$Ti_3C_2T_x$	Active materials	353.9 mAh g^{-1} at 0.1A g^{-1}	[13]
TiO_2/T-Ti_3C_2	Active materials	167.6 mAhg^{-1} at 0.5A g^{-1}	[14]
SnS_2/$Ti_3C_2T_x$	Active materials	462.1 mAh g^{-1} at 0.1 A g^{-1}	[15]
N (V)-incorporated $Ti_3C_2T_x$	Active materials	92 mAh g^{-1} at 3 C	[16]
$LiMn_2O_4$/$Ti_3C_2T_x$	Conductive coating	114.1 mAh g^{-1} at 1 C	[17]
MoS_2/$Mo_2TiC_2T_x$	Conductive substrate	572 mAh g^{-1} at 0.05 A g^{-1}	[18]
Ag/$Ti_3C_2T_x$	Conductive substrate	310.0 mAh g^{-1} at 1 C	[19]
TiO_2 nanorods/Ti_3C_2	Conductive substrate	138 mAh g^{-1} at 2 A g^{-1}	[20]

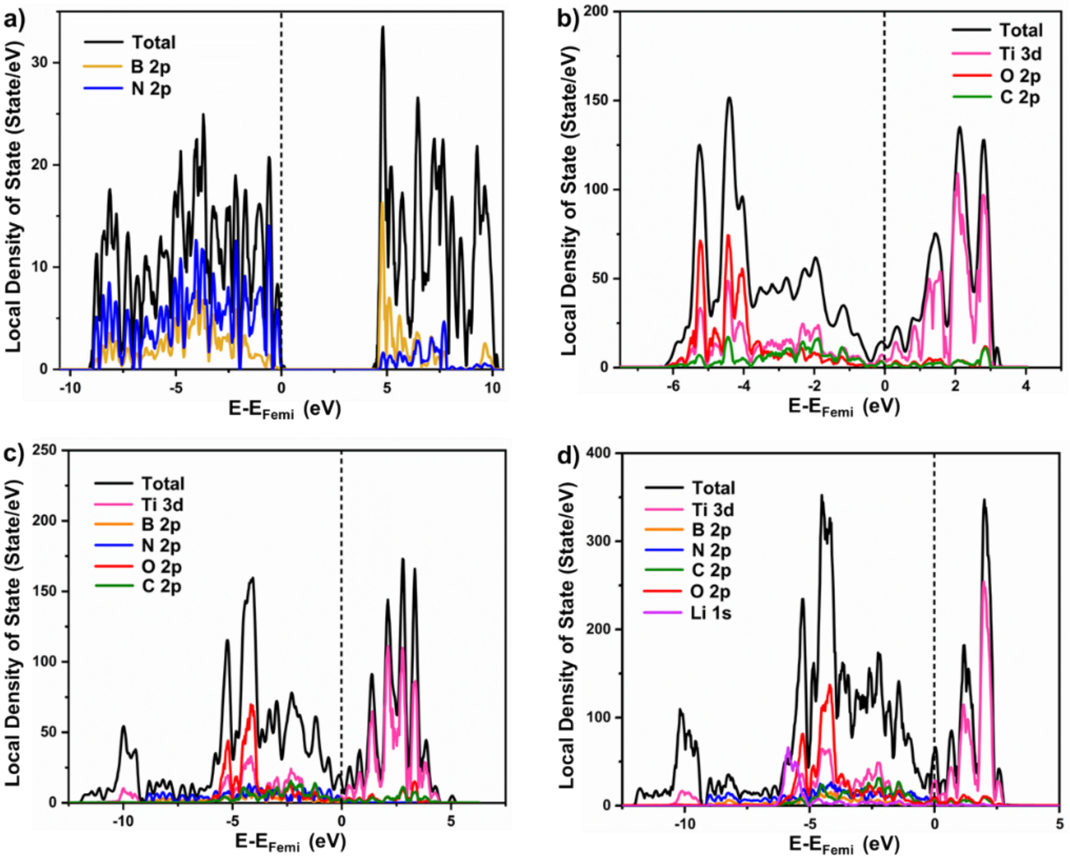

Figure S7. The calculated DOS of (a) BN, (b) $Ti_3C_2O_2$, (c) $Ti_3C_2O_2$/BN heterojunction and (d) $Ti_3C_2O_2$/BN heterojunction embedded by Li atom. The Fermi energy was set at 0 eV.

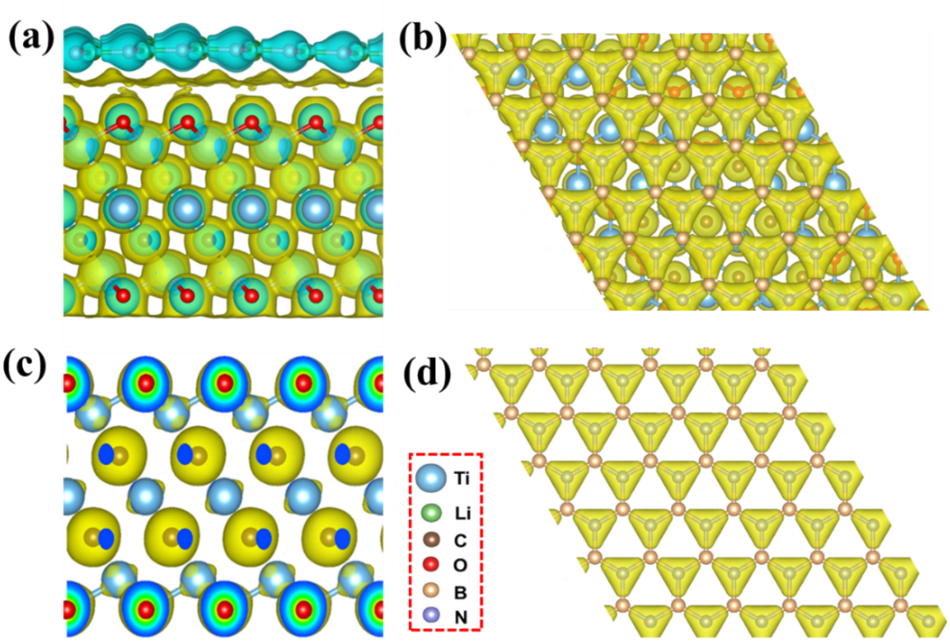

Figure S8. Charge density difference of (a-b) $Ti_3C_2T_x$/BNNSs at isovalue of 0.11 |e|/Bohr^3; (c) $Ti_3C_2T_x$ at isovalue of 0.08 |e|/Bohr^3; (d) BNNSs at isovalue of 0.13 |e|/Bohr^3; yellow and blue indicate electron accumulation and depletion, respectively.

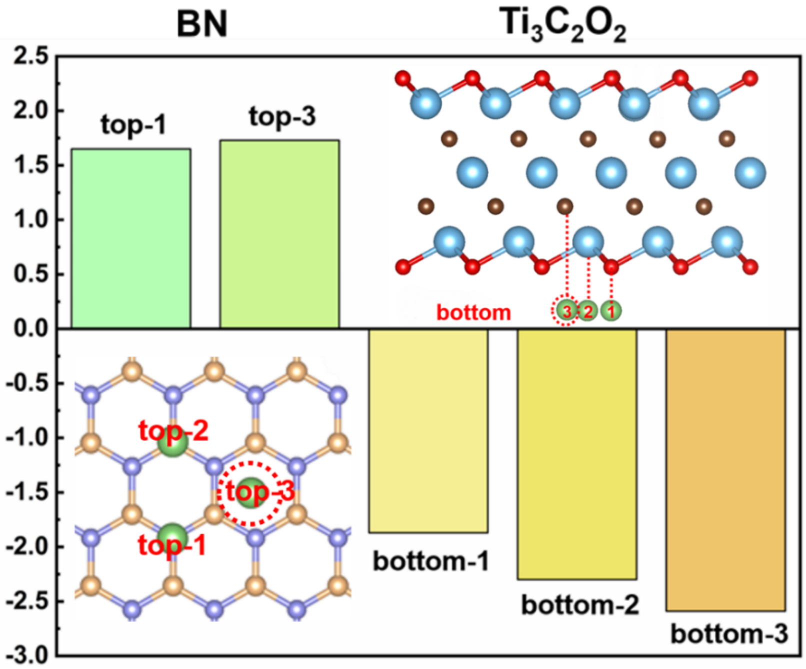

Figure S9. Top and side view of Li adsorption sites and energies on BN and $Ti_3C_2O_2$. The dashed circles denote the energetically favored adsorption sites.

As shown in Figure 5 and S9, there are three classes and each has three high symmetry adsorption sites: i) on the BN upper surface, hollow site (top-3), top site of N (top-1) and top site of B (top-2); ii) on the $Ti_3C_2O_2$ bottom surface, top site of O (bottom-1), top site of Ti (bottom-2), and top site of C (bottom-3); iii) at the BN/$Ti_3C_2O_2$ interface, top site of O (mid-1), top site of Ti (mid-2), and top site of C (mid-3). After structural optimizations, it turned out that the Li atom preferred the location at the hollow site on top of the C atom. In addition, the mid-1, mid-2, top-1 and top-2 configuration were optimized to the mid-3 and top-3 configuration, respectively.

According to the definition of E_{ad}, it could be concluded that the lithium adsorption on BN surface was poor, resulting in the growth of lithium dendrite. Surprisingly, the lithium adsorption sites and energies on $Ti_3C_2O_2$ monolayer were identical with those of BN/$Ti_3C_2O_2$ heterostructures.

References

(1) Sun, N.; Guan, Z.; Zhu, Q.; Anasori, B.; Gogotsi, Y.; Xu, B. Enhanced Ionic Accessibility of Flexible MXene Electrodes Produced by Natural Sedimentation. *Nano-micro lett.* **2020**, 12 (1), 89.

(2) Lin Z.; Sun D.; Huang Q.; Barsoum M. W.; Yan X.; Yang J. Carbon nanofiber bridged two-dimensional titanium carbide as a superior anode for lithium-ion batteries. *J. Mater. Chem. A* **2015**, 3 (27), 14096-14100.

(3) Zhang, C. J.; Kim, S. J.; Ghidiu, M.; Zhao, M.-Q.; Barsoum, M. W.; Nicolosi, V.; Gogotsi, Y. Layered Orthorhombic Nb_2O_5@$Nb_4C_3T_x$ and TiO_2@$Ti_3C_2T_x$ Hierarchical

Composites for High Performance Li-ion Batteries. *Adv. Funct. Mater.* **2016**, 26 (23), 4143-4151.

(4) Anasori B.; Xie Y.; Beidaghi M.; Lu J.; Hosler B. C.; Hultman L.; Kent P. R. C.; Gogotsi Y.; Barsoum M. W. Two-Dimensional, Ordered, Double Transition Metals Carbides (MXenes). *ACS Nano* **2015**, 9 (10), 9507-9516.

(5) Du, F.; Tang, H.; Pan, L.; Zhang, T.; Lu, H.; Xiong, J.; Yang, J.; Zhang, C. Environmental Friendly Scalable Production of Colloidal 2D Titanium Carbonitride MXene with Minimized Nanosheets Restacking for Excellent Cycle Life Lithium-Ion Batteries. *Electrochim. Acta* **2017**, 235, 690-699.

(6) Ma, Z.; Zhou, X.; Deng, W.; Lei, D.; Liu, Z. 3D Porous MXene (Ti3C2)/Reduced Graphene Oxide Hybrid Films for Advanced Lithium Storage. *ACS Appl. Mater. Interfaces* **2018**, 10 (4), 3634-3643.

(7) Wu, J.; Wang, Y.; Zhang, Y.; Meng, H.; Xu, Y.; Han, Y.; Wang, Z.; Dong, Y.; Zhang, X. Highly safe and ionothermal synthesis of Ti3C2 MXene with expanded interlayer spacing for enhanced lithium storage. *J. Energy Chem.* **2020**, 47, 203-209.

(8) Li, Z.; Chen, G.; Deng, J.; Li, D.; Yan, T.; An, Z.; Shi, L.; Zhang, D. Creating Sandwich-like Ti_3C_2/TiO_2/rGO as Anode Materials with High Energy and Power Density for Li-Ion Hybrid Capacitors. *ACS Sustainable Chem. Eng.* **2019**, 7 (18), 15394-15403.

(9) Kim, S. J.; Naguib, M.; Zhao, M.; Zhang, C.; Jung, H.-T.; Barsoum, M. W.; Gogotsi, Y. High mass loading, binder-free MXene anodes for high areal capacity Li-ion batteries. *Electrochim. Acta* **2015**, 163, 246-251.

(10) Lu, M.; Li, H.; Han, W.; Chen, J.; Shi, W.; Wang, J.; Meng, X.-M.; Qi, J.; Li, H.; Zhang, B.; et al. 2D titanium carbide (MXene) electrodes with lower-F surface for high performance lithium-ion batteries. *J. Energy Chem.* **2019**, 31, 148-153.

(11) Meng, R.; Huang, J.; Feng, Y.; Zu, L.; Peng, C.; Zheng, L.; Zheng, L.; Chen, Z.; Liu, G.; Chen, B.; et al. Black Phosphorus Quantum Dot/Ti3C2MXene Nanosheet Composites for Efficient Electrochemical Lithium/Sodium-Ion Storage. *Adv. Energy Mater.* **2018**, 8 (26), 1801514.

(12) Huang, H.; Cui, J.; Liu, G.; Bi, R.; Zhang, L. Carbon-Coated MoSe2/MXene Hybrid Nanosheets for Superior Potassium Storage. *ACS Nano* **2019**, 13 (3), 3448-3456.

(13) Wang, F.; Wang, Z.; Zhu, J.; Yang, H.; Chen, X.; Wang, L.; Yang, C. Facile synthesis SnO_2 nanoparticle-modified Ti_3C_2 MXene nanocomposites for enhanced lithium storage application. *J. Mater. Sci.* **2016**, 52 (7), 3556-3565.

(14) Jia, L.; Li, Y.; Su, L.; Liu, D.; Fu, Y.; Li, J.; Yan, X.; He, D. TiO_2 Nanoparticles In Situ Formed on Ti_3C_2 Nanosheets by a One-Step Ethanol-Thermal Method for Enhanced Reversible Lithium-Ion Storage. *ChemistrySelect* **2020**, 5 (10), 3124-3129.

(15) Liu, H.; He, Y.; Zhang, H.; Wang, S.; Cao, K.; Jiang, Y.; Liu, X.; Jing, Q.-S. Heterostructure engineering of ultrathin SnS_2/Ti3C2T nanosheets for high-performance potassium-ion batteries. *J. Colloid Interface Sci.* **2022**, 606, 167-176.

(16) Cheng, R.; Wang, Z.; Cui, C.; Hu, T.; Fan, B.; Wang, H.; Liang, Y.; Zhang, C.; Zhang, H.; Wang, X. One-Step Incorporation of Nitrogen and Vanadium between Ti3C2Tx MXene Interlayers Enhances Lithium Ion Storage Capability. *J. Phys. Chem.*

C **2020**, 124 (11), 6012-6021.

(17) Wei, C.; Fei, H.; An, Y.; Zhang, Y.; Feng, J. Crumpled $Ti_3C_2T_x$ (MXene) nanosheet encapsulated $LiMn_2O_4$ for high performance lithium-ion batteries. *Electrochim. Acta* **2019**, 309, 362-370.

(18) Chen, C.; Xie, X.; Anasori, B.; Sarycheva, A.; Gogotsi, Y. MoS_2-on-MXene heterostructures as highly reversible anode materials for lithium-ion batteries. *Angew. Chem., Int. Ed.* **2018**, 57 (7), 1846.

(19) Zou G. D.; Zhang Z. W.; Guo J. X.; Liu B. Z.; Zhang Q. R.; Fernandez C.; Peng Q. M. Synthesis of MXene/Ag Composites for Extraordinary Long Cycle Lifetime Lithium Storage at High Rates. *ACS Appl. Mater. Interfaces* **2016**, 8 (34), 22280-22286.

(20) Liu, Y. T.; Zhang, P.; Sun, N.; Anasori, B.; Zhu, Q. Z.; Liu, H.; Gogotsi, Y.; Xu, B. Self-Assembly of Transition Metal Oxide Nanostructures on MXene Nanosheets for Fast and Stable Lithium Storage. *Adv. Mater.* **2018**, 30 (23), e1707334.